ACS Catalysis

pubs.acs.org/acscatalysis

Research Article

Essential Roles of Cp Ring Activation and Coordinated Solvent During Electrocatalytic H_2 Production with Fe(Cp^{N3}) Complexes

Bhumika Goel, Hagen Neugebauer, Andrew I. VanderWeide, Práxedes Sánchez, Roger A. Lalancette, Stefan Grimme, Andreas Hansen,* and Demyan E. Prokopchuk*

Cite This: *ACS Catal.* 2023, 13, 13650−13662

Read Online

ACCESS | Metrics & More | Article Recommendations | Supporting Information

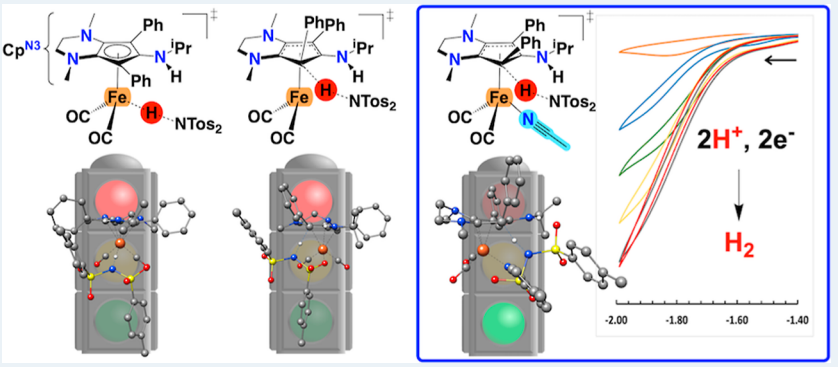

ABSTRACT: Cyclopentadienyl (Cp), a classic ancillary ligand platform, can be chemically noninnocent in electrocatalytic H−H bond formation reactions via protonation of coordinated η^5-Cp ligands to form η^4-CpH moieties. However, the kinetics of η^5-Cp ring protonation, ligand-to-metal (or metal-to-ligand) proton transfer, and the influence of solvent during H_2 production electrocatalysis remain poorly understood. We report in-depth kinetic details for electrocatalytic H_2 production with Fe complexes containing amine-functionalized $\mathbf{Cp^{N3}}$ ligands that are protonated via exogenous acid to generate via η^4-$\mathbf{Cp^{N3}H}$ intermediates ($\mathbf{Cp^{N3}}$ = 6-amino-1,4-dimethyl-5,7-diphenyl-2,3,4,6-tetrahydrocyclopenta[*b*]pyrazin-6-yl). Under reducing conditions, state-of-the-art DFT calculations reveal that a coordinated solvent plays a crucial role in mediating stereo- and regioselective proton transfer to generate ($\mathbf{\textit{endo}\text{-}Cp^{N3}H}$)$\mathbf{Fe(CO)_2(NCMe)}$, with other protonation pathways being kinetically insurmountable. To demonstrate regioselective *endo*-$Cp^{N3}H$ formation, the isoelectronic model complex ($\mathbf{\textit{endo}\text{-}Cp^{N3}H}$)$\mathbf{Fe(CO)_3}$ is independently prepared, and kinetic studies with the on-cycle hydride intermediate $\mathbf{Cp^{N3}FeH(CO)_2}$ under CO cleanly furnish the ring-activated complex ($\mathbf{\textit{endo}\text{-}Cp^{N3}H}$)$\mathbf{Fe(CO)_3}$ via metal-to-ligand proton migration. The on-cycle complex $\mathbf{Cp^{N3}FeH(CO)_2}$ reacts with acid to release H_2 and regenerate $\mathbf{[Cp^{N3}Fe(CO)_2(NCMe)]^+}$, which was found to be the TOF-determining step via DFT. Collectively, these experimental and computational results underscore the emerging importance of Cp ring activation, inner-sphere solvation, and metal−ligand cooperativity to perform proton-coupled electron transfer catalysis for chemical fuel synthesis.

KEYWORDS: *electrocatalysis, cyclopentadiene, noninnocent ligands, computational modeling, reaction mechanisms, chemical fuels*

INTRODUCTION

There is sustained interest in developing Earth-abundant electrocatalysts for chemical energy conversion that rival the activity, robustness, and efficiency of precious metals,[1] particularly since heterogenized platinum group metals are most commonly employed in H_2 electrolysis and fuel cell systems.[2−4] As an alternative to heterogeneous electrocatalyst design, molecular (homogeneous) transition-metal complexes enable the atomically precise tuning of primary, secondary, and outer coordination spheres, allowing for the interrogation of reaction mechanisms using solution-phase mechanistic tools and state-of-the-art computational protocols. For example, molecular electrocatalysts with proton-responsive ligand features, as found in naturally occurring hydrogenases,[5−7] have been used for H_2 production/oxidation[8−13] and CO_2 reduction[14−20] in combination with Earth-abundant metals. This concept has been extended to a wide range of ligand scaffolds for electrocatalytic small-molecule activation reactions, and it has been firmly established that ligand frameworks containing appended amines or alcohols facilitate cooperativity between the metal center and ligand, which increases reaction

Received: June 27, 2023
Revised: September 2, 2023

Scheme 1. Proposed Electrocatalytic H_2 Production Mechanism Including Newly Obtained Mechanistic Data (Solid Boxes) through Experimental and Computational Analysis[a]

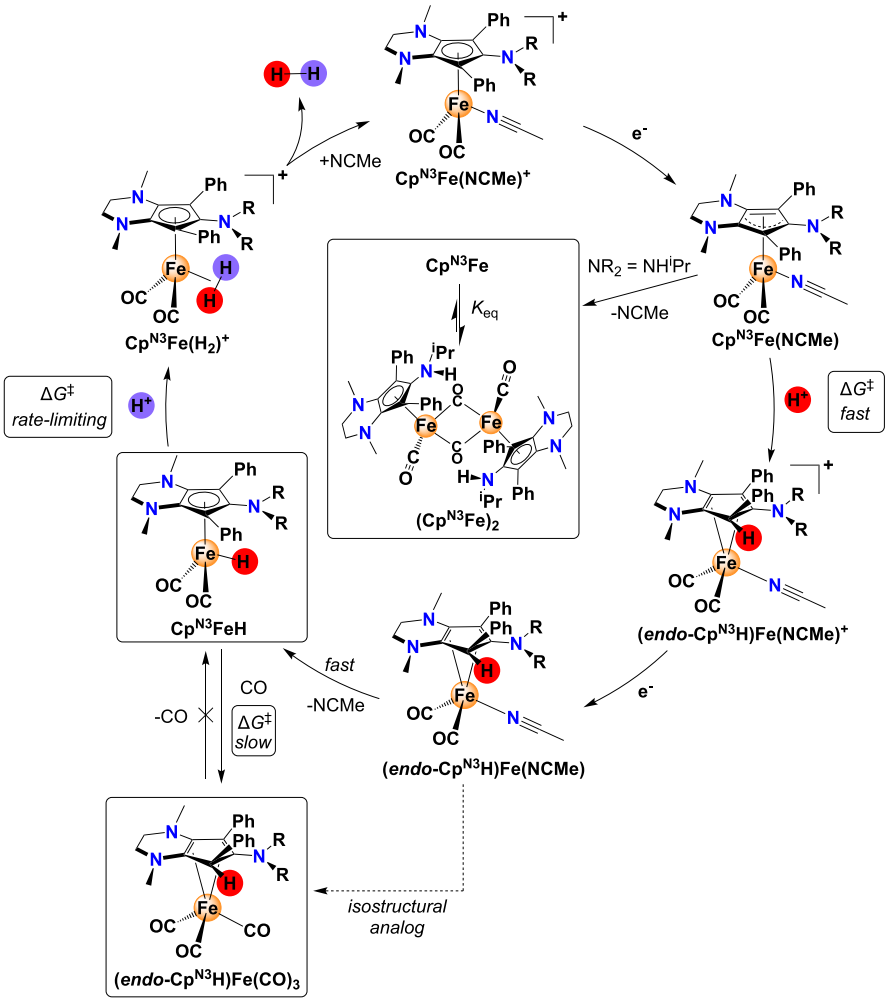

[a]NR_2 = NH^iPr, Pyrrolidynyl.

rates and/or offers new bond activation pathways.[9,20,21] In many cases, density functional theory (DFT) calculations have also been used to complement experimental findings and predict electrocatalyst properties by accurately computing free-energy landscapes.[22−24]

In contrast to ligand scaffolds containing proton-responsive O−H and N−H bonds, using ligand-based C−H bonds for proton-coupled electron transfer (PCET) applications with Earth-abundant metals remains scant. Only recently, C−H bonds within the classic "ancillary" η^5-cyclopentadienyl (Cp) ligand family have been utilized for PCET chemistry, where the η^5-Cp ligand is transformed into a dearomatized η^4-cyclopentadiene (η^4-CpH) moiety via nucleophilic or electrophilic activation.[25] Peters and co-workers reported that reactions of decamethylcobaltocene (Cp^*_2Co) and decamethylcobatocenium ($[Cp^*_2Co]^+$) with Brønsted acids and $NaBH_4$, respectively, produce (η^4-Cp*H) intermediates that release potent $H^\bullet$ or H^- moieties during the Fe-catalyzed reduction of N_2 to NH_3.[26−28] Dempsey and co-workers recently investigated the stoichiometric proton transfer kinetics with piano-stool complexes $[CpCo^{III}(diphosphine)(NCMe)]^{2+}$ under reducing conditions to understand the relationship between the kinetics of Co^{III}−H formation and the strength of exogenous acid.[29] Interestingly, the rate constant became pK_a-independent with stronger acids, and in this regime the protonation rate was gated by the rate of initial MeCN dissociation from the 1e$^-$ reduction intermediate $[CpCo^{II}(diphosphine)(NCMe)]^+$. Not only was solvent dissociation a key rate-limiting factor under these conditions, but Cp ligand protonation followed by rapid metal-to-ligand proton migration via $[(\eta^4\text{-CpH})Co^{I}(diphosphine)]^+$ was kinetically preferred over direct protonation of the Co^I center to yield the cationic Co^{III}−H adduct. Blakemore and co-workers recently reported detailed kinetic studies of the elementary reaction steps for the H_2 production electrocatalyst $Cp^*Rh^I(bpy)$ ($Cp^* = C_5Me_5$; bpy = 2,2-bipyridyl) and studied the metal−ligand tautomerization behavior for $[Cp^*Rh^{III}H(bpy)]^+ \rightleftharpoons [(\eta^4\text{-Cp*H})Rh^I(bpy)]^+$.[30] In contrast to the aforementioned Co systems, direct metal protonation with an exogenous acid is preferred (k = 6400 M^{-1} s^{-1}) instead of Cp* protonation. These divergent results suggest that ligand protonation via exogenous acid is kinetically preferable with Earth-abundant metals; however, the scarcity of kinetic studies in this area of research makes it difficult to draw any broader conclusions.

Our foray into the chemically noninnocent behavior of Cp ligands began with the investigation of H_2 production electrocatalysis using monometallic Fe complexes containing

https://doi.org/10.1021/acscatal.3c02911
ACS Catal. 2023, 13, 13650−13662

amine-rich Cp^{N3} ligands.[31] Electrochemical studies revealed that a series of piano-stool iron complexes $\mathbf{Cp^{N3}Fe(NCMe)^+}$ are active for electrocatalytic H_2 production, reaching turnover frequencies of up to 45 s^{-1} ($\mathbf{Cp^{N3}}$ = 6-amino-1,4-dimethyl-5,7-diphenyl-2,3,4,6-tetrahydrocyclopenta[*b*]pyrazin-6-yl); Scheme 1. Based solely on an exhaustive free energy landscape analysis of computationally derived pK_a and electrochemical measurements, our key mechanistic insight was that the amines were not directly involved in proton transfer, and stereospecific *endo*-Cp ring protonation occurs after 1e$^-$ reduction, breaking the η^5 hapticity to generate an $\mathbf{(\textit{endo}\text{-}Cp^{N3}H)Fe(NCMe)^+}$ intermediate. Using acid−base arguments, solvent coordination was posited at this stage, with $\mathbf{(\textit{endo}\text{-}Cp^{N3}H)Fe(NCMe)^+}$ being the only plausible option (pK_a^{MeCN} = 15.7), given the acidity of the exogenous acid (Tos_2NH; pK_a^{MeCN} = 11.97)[32] during catalysis.[31] Next, ligand-to-metal proton migration was proposed to occur after a second reduction to generate the hydride complex $\mathbf{Cp^{N3}FeH}$, followed by direct protonation of $\mathbf{Cp^{N3}FeH}$, liberating H_2 and regenerating $\mathbf{Cp^{N3}Fe(NCMe)^+}$. However, no experimental evidence for Cp ring activation was presented, and kinetic analyses were not undertaken to further support this unexpected reaction pathway.

In this, we expand significantly on our initial mechanistic understanding of this reaction by using a suite of spectroscopic and computational techniques that rationalize the observed kinetics data, provide strong support for Cp ring activation, and highlight the crucial role of solvent coordination during electrocatalysis (Scheme 1, solid boxes). We show that using a slightly stronger acid in acetonitrile boosts electrocatalytic H_2 production by 5-fold (up to 266 s^{-1}); however, switching the reaction medium to isobutyronitrile (^{i}PrCN) or *N*,*N*-dimethylformamide (DMF) suppresses catalysis, indicating that solvent (acetonitrile) association in the primary coordination sphere is essential to facilitate catalytic turnovers. The hydride intermediate $\mathbf{Cp^{N3}FeH}$ is independently prepared and structurally validated, and DFT calculations indicate that direct protonation of $\mathbf{Cp^{N3}FeH}$ with exogenous acid is turnover-limiting during electrocatalysis. State-of-the-art computational workflows demonstrate that stereo- and regioselective ligand protonation is kinetically facile to generate $\mathbf{(\textit{endo}\text{-}Cp^{N3}H)Fe(NCMe)}$ during catalysis, followed by solvent dissociation and highly exothermic ligand-to-metal proton transfer to generate $\mathbf{Cp^{N3}FeH}$. Computed pathways involving direct metal protonation or ligand protonation in the absence of a coordinated solvent are kinetically insurmountable. To indirectly support the ligand-based protonation behavior during catalysis, the isoelectronic analogues $\mathbf{(\textit{endo}\text{-}Cp^{N3}H)Fe(CO)_3}$ are synthesized (NR_2 = NH^{i}Pr, Pyrr), both of which are structurally authenticated via single-crystal X-ray diffraction. DFT-based kinetic data show that substitution of CO for NCMe dramatically decreases the rate of ligand-to-metal proton transfer, going from $\Delta G^{\ddagger} \cong 5$ kcal/mol (NCMe) to $\Delta G^{\ddagger} \cong 34$ kcal/mol (CO), providing a clear rationale for the rapid ligand-to-metal proton migration behavior during catalysis. Experimental kinetic data show that the reverse reaction to produce $\mathbf{(\textit{endo}\text{-}Cp^{N3}H)Fe(CO)_3}$ from $\mathbf{Cp^{N3}FeH}$ is quantitative in the presence of CO, supporting the *endo*-selective proton migration behavior. Infrared spectroelectrochemistry (IR-SEC) and stoichiometric reduction reactions reveal that an off-cycle CO-bridged dimer $\mathbf{(Cp^{N3}Fe)_2}$ is formed in the absence of an exogenous acid, which is characterized via single-crystal X-ray diffraction and solution-phase equilibrium measurements. Collectively, these results underscore the novelty and importance of Cp ring activation, inner-sphere solvation, and metal−ligand cooperativity to perform PCET catalysis for chemical fuel synthesis.

RESULTS AND DISCUSSION

Influence of Acid and Solvent on Electrocatalysis. Our initial report[31] surveyed H_2 production electrocatalysis using Tos_2NH (pK_a^{MeCN} = 11.97)[32] as the exogenous acid since many other commonly used exogenous acids produced significant amounts of background current at potentials beyond −1.6 V.[33] We found that the slightly stronger acid dibenzenesulfonamide ($(PhSO_2)_2NH$; pK_a^{MeCN} = 11.35)[32] is also compatible in the applied potential window (Figure S16). Thus, complexes $\mathbf{1\text{-}Cp^{N3}Fe(NCMe)^+}$ (NR_2 = NH^{i}Pr) and $\mathbf{2\text{-}Cp^{N3}Fe(NCMe)^+}$ (NR_2 = Pyrrolidinyl) were tested with $(PhSO_2)_2NH$ for H_2 production electrocatalysis using cyclic voltammetry (CV) at ≥800 mV/s to observe current responses that are independent of scan rate.[31] When $\mathbf{1\text{-}Cp^{N3}Fe(NCMe)^+}$ is treated with increasing concentrations of $(PhSO_2)_2NH$, the plateau current increases when $[(PhSO_2)_2NH] \leq 100$ mM (Figure 1, inset). In the kinetic regime where the current response is independent of $[(PhSO_2)_2NH]$, the observed rate constant k_{obs} = 118 s^{-1} for H_2 production at an estimated overpotential of 1.04 V (Table 1).[34] Next, $\mathbf{2\text{-}Cp^{N3}Fe(NCMe)^+}$ was tested for catalysis with $(PhSO_2)_2NH$, resulting in k_{obs} = 266 s^{-1} for H_2 production at an estimated overpotential of 1.12 V (Figure 1 and Table 1). Therefore, an increase in acidity by 0.6 pK_a units results in a 4-fold increase in activity for $\mathbf{1\text{-}Cp^{N3}Fe(NCMe)^+}$ and 8-fold increase for $\mathbf{2\text{-}Cp^{N3}Fe(NCMe)^+}$, respectively. Controlled potential electrolysis (CPE) with exogenous acid and electrocatalyst over the course of 30 min shows sustained current output and a persistent yellow color; however, Faradaic efficiencies (FE) below unity are found in both cases (Table 1). Based on control experiments in the absence of Fe complex, we attribute this to slow decomposition of the exogenous acid during CPE (see the Supporting Information). Although rinse tests alone do not conclusively exclude the formation of heterogeneously adsorbed metal catalysts,[35,36] performing a rinse test using a freshly prepared 20 mM $(PhSO_2)_2NH$ solution reveals a similar current response and FE in comparison to control CPE experiments with a freshly polished electrode dipped into solutions containing 20 mM $(PhSO_2)_2NH$ in the absence of an electrocatalyst (Figure S25 and Table S1).

To probe the effect of isotopic labeling on the kinetics of H_2 production, deuterium-substituted 4-methyl-*N*-tosylbenzenesulfonamide (Tos_2ND) was synthesized (Figure S12) and used as the exogenous acid with $\mathbf{1\text{-}Cp^{N3}Fe(NCMe)^+}$. Successive additions of acid showed significantly lower current enhancements with k_{obs} = 22 s^{-1} when $[Tos_2ND]$ = 60 mM (Figure S17) when compared with Tos_2NH (k_H/k_D = 1.33). This normal kinetic isotope effect (KIE) suggests that H^+ transfer is involved in the rate-determining step.[37] Using DFT (see the Supporting Information for details), the computed free-energy barriers of direct protonation of $\mathbf{1\text{-}Cp^{N3}FeH}$ and $\mathbf{2\text{-}Cp^{N3}FeH}$ are consistent with this finding (Table 1) and in good agreement with the observed rates ($\Delta\Delta G^{\ddagger}$ = 0.7 to 1.9 kcal/mol; Figure 2). DFT rate constants were obtained from conventional transition-state theory with the r^{2}SCAN0-D4/def2-QZVPP level of theory employing the Eyring equation under the assumption that the transmission coefficient equals one. Although the computed rate constants are lower than the experimentally observed values, the general trend has been

https://doi.org/10.1021/acscatal.3c02911
ACS Catal. 2023, 13, 13650−13662

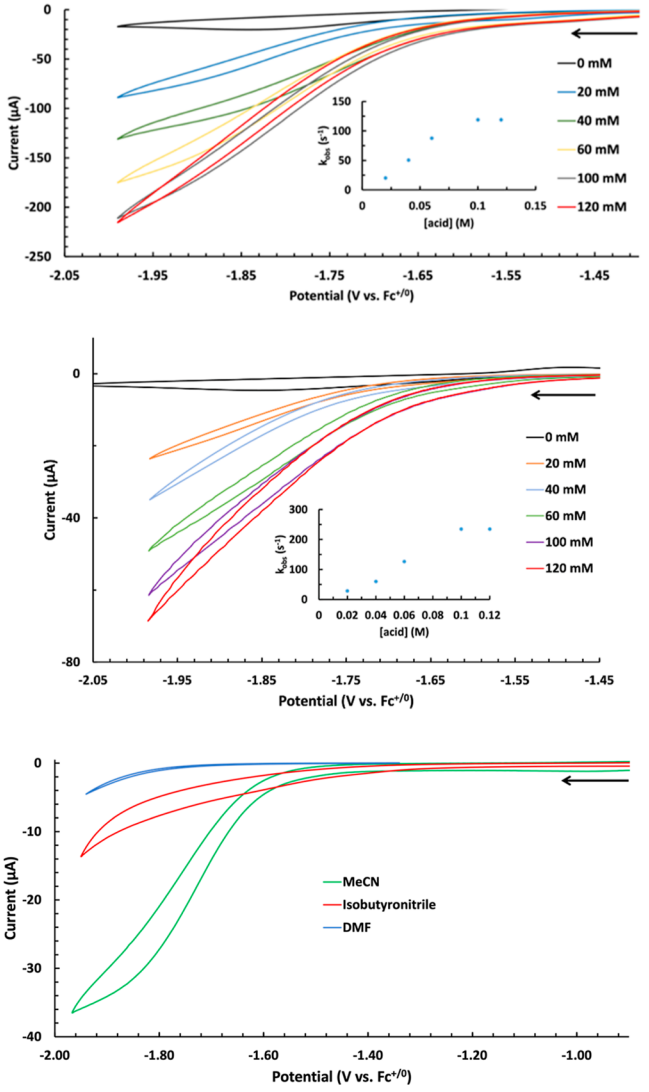

Figure 1. IUPAC plotted, *iR* uncompensated CV traces of **1-Cp^{N3}Fe(NCMe)$^+$** (top) and **2-Cp^{N3}Fe(NCMe)$^+$** (middle) with increasing concentrations of $(PhSO_2)_2NH$ at 800 mV/s with inset plots showing dependence of k_{obs} on acid concentration. (Bottom) Comparison of electrocatalytic current responses with 1 mM **1-Cp^{N3}Fe(NCMe)$^+$** dissolved in MeCN, *N*,*N*-dimethylformamide (DMF), or isobutyronitrile in the presence of 20 mM Tos_2NH at 800 mV/s. Conditions: Ar, MeCN solvent, 0.1 M $[Bu_4N][PF_6]$, 1.0 mM analyte, PEEK-encased glassy carbon working electrode, Type 2 glassy carbon rod counter electrode, and Ag/AgCl pseudoreference electrode in a frit-separated (CoralPor) glass compartment containing solvent and electrolyte. Initial scan direction and starting position indicated with a black arrow.

reproduced, showing that the stronger acid $(PhSO_2)_2NH$ lowers the free-energy barrier for protonation. Considering

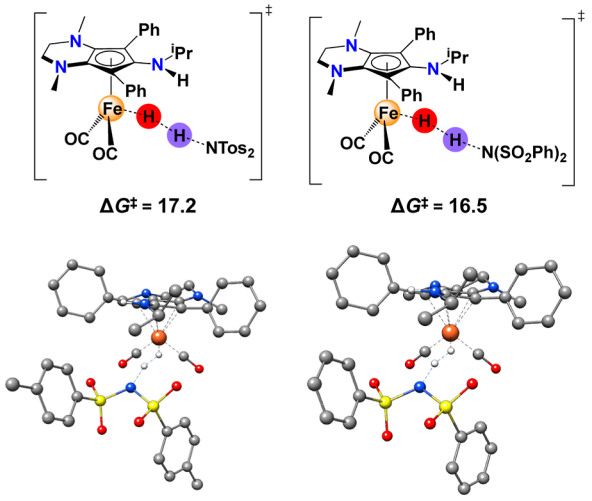

Figure 2. Computed transition states for the direct protonation of **1-Cp^{N3}FeH** to generate **1-Cp^{N3}Fe(H$_2$)$^+$** via Tos_2NH (left) and $(PhSO_2)_2NH$ (right). Energies are given in kcal/mol.

that small errors for reaction barriers of 1 kcal/mol lead to a factor of around 10 in the rate constants[38] and typical DFT errors for transition-metal barrier heights are around 2 kcal/mol with the best performing DFT methods,[39,40] the rate constants from the experiment and DFT in Table 1 are in reasonable agreement.[41]

Next, we explored the effect of solvent on current response in the presence and absence of exogenous acid by dissolving **1-Cp^{N3}Fe(NCMe)$^+$** in *N*,*N*-dimethylformamide (DMF) or isobutyronitrile (^{i}PrCN). We presume that the coordinated NCMe ligand of **1-Cp^{N3}Fe(NCMe)$^+$** is immediately replaced by DMF or ^{i}PrCN in solution. In the absence of acid, CVs of **1-Cp^{N3}Fe(NCMe)$^+$** in DMF and ^{i}PrCN show irreversible reduction waves at E_{pc} = −1.72 and −1.83 V, respectively (Figure S18), suggesting that solvent dissociation from the metal's primary coordination sphere is rapid since an anodic wave appears in MeCN. Compared to the CV of **1-Cp^{N3}Fe(NCMe)$^+$** in MeCN (E_{pc} = −1.72 V), the cathodic peak potential in DMF is nearly identical, while the potential in ^{i}PrCN is 110 mV more negative due to its slightly increased donicity (basicity). Next, CVs were conducted with **1-Cp^{N3}Fe(NCMe)$^+$** in the presence of 20 mM Tos_2NH, and almost no current enhancement is observed in DMF while a modest increase is seen using ^{i}PrCN (Figure 1 bottom and Figure S19). This strongly indicates that the presence of MeCN in the primary coordination sphere of Fe is crucial for rapid electrocatalysis.

Using DFT, we investigated the protonation free energy barriers under three different scenarios: (1) protonation at the *endo*-CpH position of **1-Cp^{N3}Fe(NCMe)** with $\Delta G^{\ddagger}$ = 9.8 kcal/mol (**TS1**); (2) dissociation of MeCN and protonation at the

Table 1. Electrocatalysis Data with 1-Cp^{N3}Fe(NCMe)$^+$ and 2-Cp^{N3}Fe(NCMe)$^+$

catalyst	acid (pK_a^{MeCN})	k_{obs}[a] (k_{DFT})[b], s^{-1}	overpotential (η), V[a]	FE (%)
1-Cp^{N3}Fe(NCMe)$^+$	Tos_2NH (11.97)	29[c] (9)	0.98[c]	65 ± 3[c]
2-Cp^{N3}Fe(NCMe)$^+$	Tos_2NH (11.97)	35[c] (4)	1.02[c]	65 ± 3[c]
1-Cp^{N3}Fe(NCMe)$^+$	$(PhSO_2)_2NH$ (11.35)	118 (34)	1.04	77 ± 2
2-Cp^{N3}Fe(NCMe)$^+$	$(PhSO_2)_2NH$ (11.35)	266 (12)	1.12	77 ± 3

[a]Calculated using standard protocols for catalytic plateau current and overpotential analysis.[42,43] [b]Computed values from $\Delta G^{\ddagger}$ for the protonation of **Cp^{N3}FeH** to form **Cp^{N3}Fe(H$_2$)$^+$**. [c]ref 31.

https://doi.org/10.1021/acscatal.3c02911
ACS Catal. 2023, 13, 13650−13662

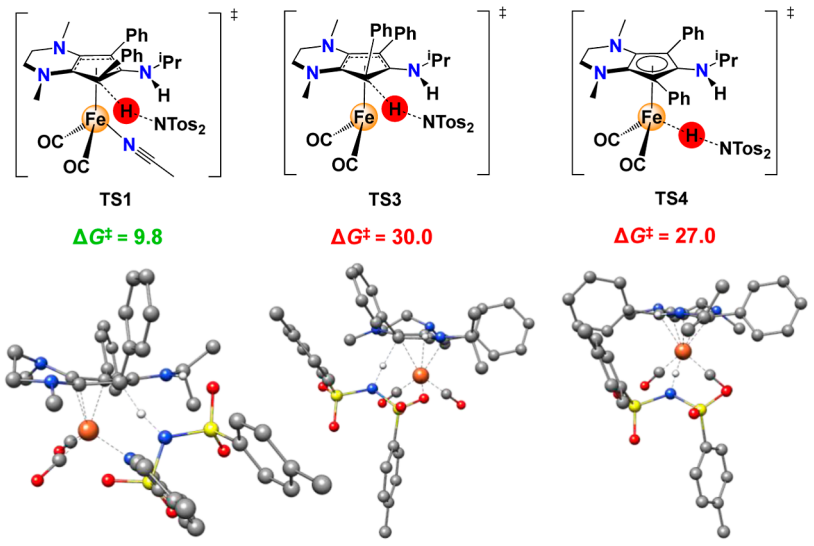

Figure 3. Free energies for three different protonation scenarios starting with **1-Cp^{N3}Fe(NCMe)**. Energies are given in kcal/mol.

Scheme 2. Synthesis and Reactivity of Cp^{N3}FeH

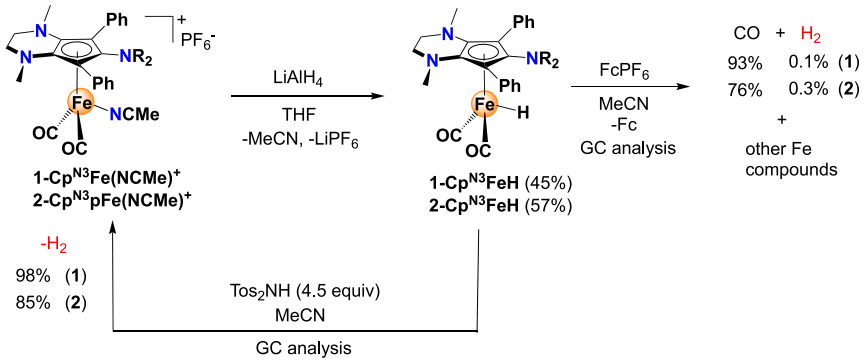

endo-CpH position of **1-Cp^{N3}Fe** with $\Delta G^{\ddagger}$ = 30.0 kcal/mol (**TS3**); and (3) dissociation of MeCN and protonation at the metal center of **1-Cp^{N3}Fe**, formally generating an Fe^{III} hydride with $\Delta G^{\ddagger}$ = 27.0 kcal/mol (**TS4**; Figure 3). Clearly, **TS3** and **TS4** are kinetically inaccessible, which is consistent with the experimentally observed solvent dependence on rapid electrocatalysis as described above. Despite many attempts, DFT modeling of similar ligand protonation transition states for complexes with the general formula **1-Cp^{N3}Fe(L)** (L = DMF, ^{i}PrCN) was unsuccessful, possibly due to the increased steric congestion, which makes the carbon atom inaccessible on the Cp^{N3} ring. A low-barrier pathway involving amine protonation at **1-Cp^{N3}Fe** was also found; however, the proton transfer barrier to form **1-Cp^{N3}FeH** is insurmountable (**TS6**, $\Delta G^{\ddagger}$ = 23.6 kcal/mol; Figure S29).

Synthesis and Reactivity of Cp^{N3}FeH Complexes. To demonstrate the release of H_2 in the final stages of the cycle, we prepared the FeH complexes shown in Scheme 1 and exposed them to exogenous acid. The FeH complexes were synthesized by taking **1-Cp^{N3}Fe(NCMe)$^+$** or **2-Cp^{N3}Fe-(NCMe)$^+$** and stirring with $LiAlH_4$ at room temperature, yielding **1-Cp^{N3}FeH** and **2-Cp^{N3}FeH** in a good yield (Scheme 2). The symmetric and asymmetric CO stretches for the carbonyl ligands appear at 1968 and 1907 cm^{-1} for **1-Cp^{N3}FeH** and 1968 and 1900 cm^{-1} for **2-Cp^{N3}FeH**. The ^{1}H NMR spectra show characteristic singlets for **1-Cp^{N3}FeH** and **2-Cp^{N3}FeH** at −10.75 and −10.72 ppm, respectively, while ^{13}C NMR spectra show singlets at 218.47 and 218.11 ppm. Single crystals suitable for X-ray diffraction reveal the molecular structures of **1-Cp^{N3}FeH** (Figure 4A) and **2-Cp^{N3}FeH** (Figure 4B). For **1-Cp^{N3}FeH**, the hydride ligand is freely refined for one of the molecules in the asymmetric unit [Fe1−H27 = 1.47(2) Å]; however, the hydride could not be located for the second Fe complex due to two-site positional disorder of the hydride and CO ligand in the asymmetric unit. The measured Fe−H bond distance is comparable to other piano-stool iron hydride complexes that have been charac-

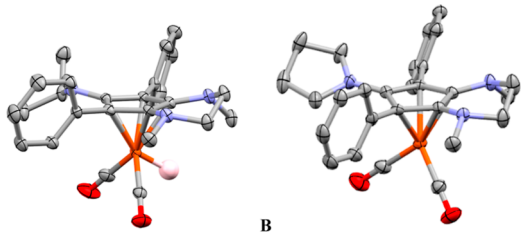

Figure 4. X-ray crystallographic structures of **1-Cp^{N3}FeH** (A) and **2-Cp^{N3}FeH** (B) with 50% probability ellipsoids. Hydrogens removed for clarity except for the hydride ligand of **1-Cp^{N3}FeH**. For **1-Cp^{N3}FeH**, the hydride could not be located for the second Fe complex in the asymmetric unit due to two-site positional disorder of the hydride and CO ligand. For **2-CpFeH**, the hydride could not be located in the Fourier difference map.

https://doi.org/10.1021/acscatal.3c02911
ACS Catal. 2023, 13, 13650−13662

terized by X-ray diffraction.[44] In the Fourier difference map of **2-Cp^{N3}FeH**, the hydride could not be located (Figure 4, right).

The reactivity of **1-Cp^{N3}FeH** and **2-Cp^{N3}FeH** was interrogated. The catalytic cycle in Scheme 1 indicates that the H_2 production loop is closed by direct protonation of **1-Cp^{N3}FeH** by Tos_2NH to generate a transient dihydrogen complex, followed by H_2 release and MeCN binding to Fe. Thus, complex **1-Cp^{N3}FeH** or **2-Cp^{N3}FeH** was reacted with 4.5 equiv Tos_2NH in a septum-sealed NMR tube under N_2, and the headspace was analyzed by gas chromatography (Scheme 2). The chromatographs reveal that **1-Cp^{N3}FeH** and **2-Cp^{N3}FeH** smoothly release H_2 in 98 and 85% yields, respectively, with no detectable formation of gaseous CO.

Next, the reactivity of **1-Cp^{N3}FeH** and **2-Cp^{N3}FeH** was evaluated under oxidizing conditions. The ligand-to-metal proton migration to form **Cp^{N3}FeH** in Scheme 1 is proposed to occur via 1-(*endo*-**Cp^{N3}H**)**Fe(NCMe)**; however, there are no experimental data ruling out ligand-to-metal proton migration from the putative radical cation **1-(*endo*-Cp^{N3}H)-Fe(NCMe)$^+$**, which would generate the intermediate **1-Cp^{N3}FeH$^+$**.[31] Thus, the anodic electrochemistry of **1-Cp^{N3}FeH** in acetonitrile was investigated. An irreversible oxidation peak is observed (E_{pc} = 0.0 V), consistent with theory ($E°$ = 0.04 V);[31] however, the peak current diminishes significantly after each CV sweep which suggests electrode fouling (Figure S20). CVs were conducted at 10 and 20 V/s with repolishing in between each run, but no return oxidation waves were detected, indicating rapid degradation of electrogenerated **1-Cp^{N3}FeH$^+$** (Figure S21). Using a weakly coordinating solvent such as fluorobenzene engenders partially reversible redox waves with **1-Cp^{N3}FeH** at scan rates greater than 5 V/s, suggesting that MeCN coordination may play a role during product decomposition (Figure S22). Finally, the oxidative degradation of **1-Cp^{N3}FeH** and **2-Cp^{N3}FeH** was further supported by treating each complex with 5 equiv ferrocenium hexafluorophosphate ($FcPF_6$) in acetonitrile under an inert atmosphere in a septum-sealed NMR tube. GC headspace analysis reveals CO gas evolution in 93 and 76% yields for **1-Cp^{N3}FeH** and **2-Cp^{N3}FeH**, respectively, with only trace amounts of H_2 (0.1−0.3%) relative to the initial [Fe]; NMR analysis of the solution phase reaction mixtures show intractable mixtures of products, while IR analysis reveals several low-intensity stretches in the carbonyl region that we were unable to confidently assign. Although many stable transition-metal hydride radical cations are known,[45] we posit that decomposition of **1-Cp^{N3}FeH$^+$** is facile, and this species does not play a role in H_2 production electrocatalysis.

Synthesis and Proton Migration Kinetics of (*endo*-Cp^{N3}H)Fe(CO)$_3$ Complexes. Thus, far, our evidence indicates that the formation of **1-Cp^{N3}FeH** likely occurs by intramolecular ligand-to-metal proton migration via (***endo*-Cp^{N3}H)Fe(NCMe)**, formally an 18e$^-$ Fe^0 complex. This *endo* stereoisomer is energetically preferred over the *exo*-Cp^{N3}H adduct by 9.6 kcal/mol,[31] presumably due to the decreased steric congestion by having the phenyl ring pointing away from the metal center and CO ligands. Although we have been unable to isolate **(*endo*-Cp^{N3}H)Fe(NCMe)**, exposure of **1-Cp^{N3}Fe(CO)$_3^+$** or **2-Cp^{N3}Fe(CO)$_3^+$** to $NaHBEt_3$ under 2.5 atm of CO in cold THF results in regio- and stereoselective *endo*-Cp ring activation to generate complexes **1-(*endo*-Cp^{N3}H)Fe** and **2-(*endo*-Cp^{N3}H)Fe** (Figure 5, top), which are isoelectronic variants of the key catalytic intermediate **(*endo*-Cp^{N3}H)Fe(NCMe)**. These complexes are very stable

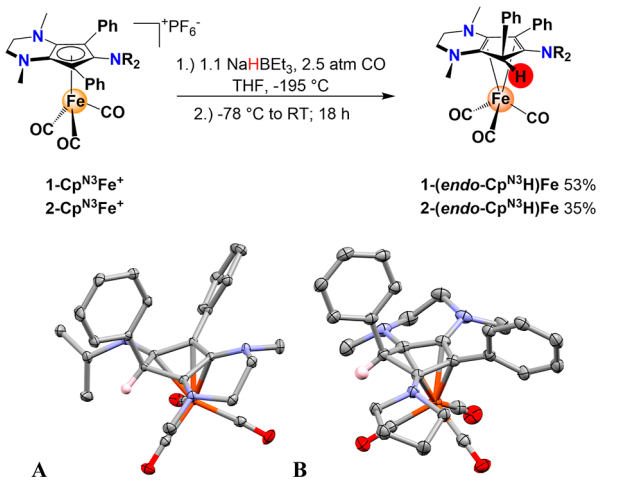

Figure 5. Top: Synthesis of ring-activated compounds **1-(*endo*-Cp^{N3}H)Fe** and **2-(*endo*-Cp^{N3}H)Fe**. Bottom: X-ray crystallographic structures of **1-(*endo*-Cp^{N3}H)Fe** (A) and **2-(*endo*-Cp^{N3}H)Fe** (B) with 50% probability ellipsoids (most hydrogens omitted for clarity).

under an inert atmosphere, but higher pressures of $CO_{(g)}$ are necessary during their synthesis to minimize CO dissociation and subsequent formation of **1-Cp^{N3}FeH** or **2-Cp^{N3}FeH**. Diagnostic ^{1}H NMR spectroscopic data for **1-(*endo*-Cp^{N3}H)-Fe** and **2-(*endo*-Cp^{N3}H)Fe** include singlets at 4.84 and 4.77 ppm, respectively, corresponding to the *endo*-Cp^{N3}H proton resonance. The presence of three CO stretches from 1978 to 1886 cm^{-1} in the IR spectra is also indicative of an increase of electron density at the metal center, as the starting complexes exhibit CO stretches from 1999 to 1940 cm^{-1}.[31]

Crystallization from ether/pentane solutions provides X-ray quality crystals, validating the molecular structures of **1-(*endo*-Cp^{N3}H)Fe** (Figure 5A) and **2-(*endo*-Cp^{N3}H)Fe** (Figure 5B). Structural analyses indicate that there is a high degree of electronic delocalization throughout the unsaturated carbon atoms of the η^4-cyclopentadiene moiety due to the formal 2e$^-$ reduction of the metal center and a greater degree of π backbonding into the butadiene motif.[46] For example, in **1-Fe(*endo*-Cp^{N3}H)**, all three C−C bonds in the diene portion of the ring are similar in length [C6−C7 = 1.428(2) Å; C7−C8 = 1.442(2) Å; C8−C4 = 1.445(2) Å], while the C−C bonds connected to the tetrahedral C5 are substantially elongated [C4−C5 = 1.530(2) Å; C6−C5 = 1.512(2) Å]. To the best of our knowledge, nucleophilic activation at an η^5-Cp ring to generate an isolable (η^4-CpH)Fe^0 complex is rare, with only three other examples reported in the literature.[47−49]

Since experimental data for the kinetics of ligand-to-metal proton migration via η^4-CpH intermediates remains scant,[29] we attempted to convert **2-(*endo*-Cp^{N3}H)Fe** into **2-Cp^{N3}FeH** to emulate the proton migration behavior during electrocatalysis via **(*endo*-Cp^{N3}H)Fe(NCMe)**. Complex **2-(*endo*-Cp^{N3}H)Fe** is very stable under inert gas at room temperature; therefore, the compound was heated in toluene-d_8 for prolonged periods of time and monitored by ^{1}H NMR. However, even after 16.5 h at 105 °C, only a trace amount of **2-Cp^{N3}FeH** was observed (<1%) along with some signal broadening, suggestive of gradual decomposition (Figure S26). Since the hydride complexes **1-Cp^{N3}FeH** and **2-Cp^{N3}FeH** are also formed as minor products during synthesis of the *endo*-CpH using $NaHBEt_3$, we hypothesized that the Lewis acidic BEt_3 might facilitate proton migration; however, addition of

https://doi.org/10.1021/acscatal.3c02911
ACS Catal. 2023, 13, 13650−13662

BEt_3 to a pure sample of **2-(*endo*-Cp^{N3}H)Fe** in CD_3CN elicited no reaction after 24 h at room temperature (Figure S27).

To obtain a clearer understanding of why **2-(*endo*-Cp^{N3}H)Fe** is so unreactive, relaxed potential energy surface scans via DFT were performed, providing the electronic energies (ΔE, kcal/mol) as a function of Fe−CO distance (Δd, Å; Figure 6). For selected points on this scan, approximate

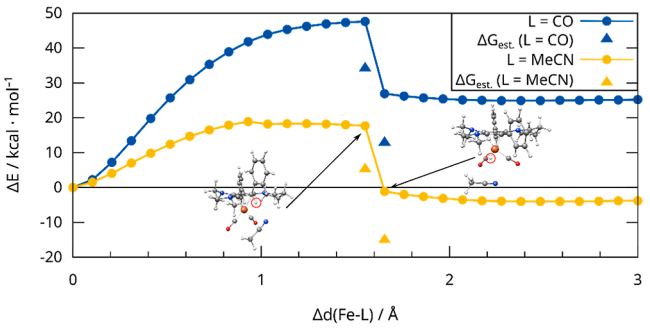

Figure 6. Relaxed surface scan performed in ORCA[50] on the PBE0-D3(BJ)/def2-SVP (def2-TZVP for Fe) + CPCM (MeCN) level of theory[51−54] going from **2-(*endo*-Cp^{N3}H)Fe** to **2-Cp^{N3}FeH** + CO (blue trace) and **2-(*endo*-Cp^{N3}H)Fe(NCMe)** to **2-Cp^{N3}FeH** + NCMe (yellow trace). The (free) energies are given relative to Δd(Fe−L) = 0. Thermostatistical corrections were added for selected nodes of the scan (blue and yellow triangles).

thermostatistical corrections were added because no clean transition state could be obtained on going from **2-Fe(*endo*-Cp^{N3}H)** to **2-Cp^{N3}FeH** (see the Supporting Information for details). Thus, all free energies discussed in this section refer to these corrected free energies. Calculations indicate that the barrier to removing CO, a strong π-acceptor, is substantial at room temperature ($\Delta G^{\ddagger}$ = 34.2 kcal/mol). In contrast, substituting CO with NCMe dramatically lowers the free-energy barrier for ligand dissociation in **(*endo*-Cp^{N3}H)Fe(NCMe)**, making the reaction very rapid under standard-state conditions ($\Delta G^{\ddagger}$ = 5.3 kcal/mol) and is therefore consistent with the observed kinetics of H_2 production electrocatalysis. Again, these data underscore the importance of acetonitrile coordination, which facilitates facile proton migration from the Cp^{N3} ligand to iron. A very similar reactivity profile was also modeled for **1-Fe(*endo*-Cp^{N3}H)** (Figure S30).

The large energy difference between **2-(*endo*-Cp^{N3}H)Fe** and **2-Cp^{N3}FeH** in Figure 6 (blue trace) suggests that the reverse reaction (i.e., metal-to-ligand proton migration) should be very exothermic under relatively mild conditions. Thus, we prepared an 18 mM solution of **2-Cp^{N3}FeH** in 0.50 mL CD_3CN and pressurized an NMR tube with 6.5 atm $CO_{(g)}$, ensuring that there was an excess (about 5 equiv) of dissolved CO relative to **2-Cp^{N3}FeH**, enabling us to model the kinetics under pseudo-first-order conditions (see the Supporting Information for details). Room-temperature monitoring via ^{1}H NMR revealed that the reaction was sluggish, with only ca. 1% conversion after 16 h. Thus, the reaction was conducted in the NMR probe at 45 °C and ^{1}H NMR spectra were automatically collected every 20 min over the course of 8 h. Very clean conversion from **2-Cp^{N3}FeH** to **2-(*endo*-Cp^{N3}H)Fe** was observed by monitoring the loss of the hydride signal at −10.72 ppm and growth of the Cp^{N3}H resonance at 4.84 ppm (Figure S28). The first-order rate constant for the disappearance of **2-Cp^{N3}FeH** (1.1×10^{-4} s^{-1}) and appearance of **2-(*endo*-Cp^{N3}H)Fe** (8.8×10^{-5} s^{-1}) yields an average rate constant $k_{obs} = 9.9 \pm 1.5 \times 10^{-4}$ s^{-1} for metal-to-ligand proton migration (Figure 7), which is in reasonable agreement with

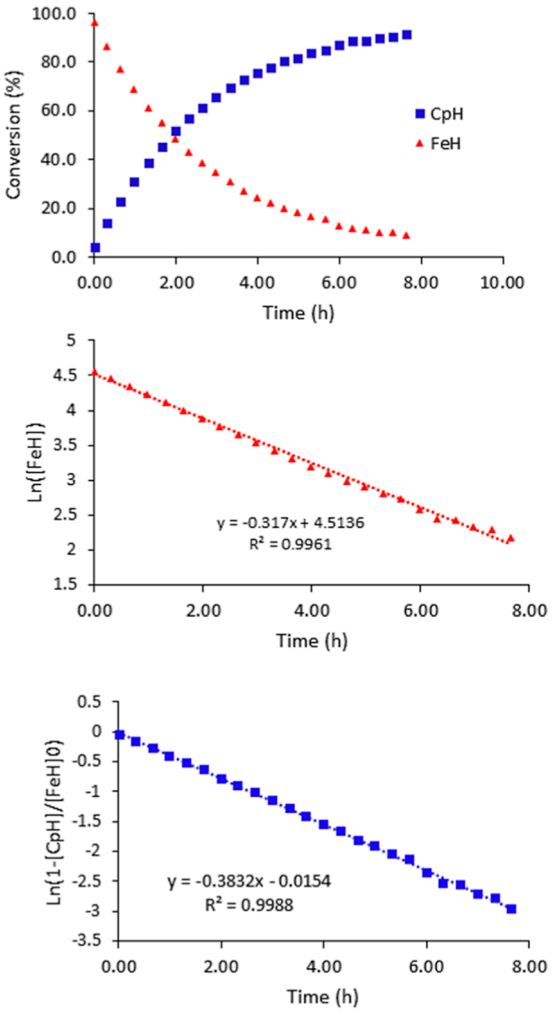

Figure 7. Kinetic traces for the conversion of **2-Cp^{N3}FeH** to **2-(*endo*-Cp^{N3}H)Fe** in CD_3CN at 45 °C. Top: Percent conversion for the appearance of **2-(*endo*-Cp^{N3}H)Fe** (blue squares) and disappearance of **2-Cp^{N3}FeH** (red triangles). Middle: First-order fit for the disappearance of **2-Cp^{N3}FeH**. Bottom: First-order fit for the appearance of **2-(*endo*-Cp^{N3}H)Fe**.

the computed barrier ($\Delta G^{\ddagger}$ = 21.2 kcal/mol; $k_{DFT} = 1.1 \times 10^{-2}$ s^{-1}), considering the approximate nature of the relaxed surface scan. Therefore, the kinetic barrier impeding ligand-to-metal proton migration in **2-(*endo*-Cp^{N3}H)Fe** is from CO ligand dissociation and the proton transfer is practically barrierless once a vacant site is available.

IR Spectroscopy and an Off-Cycle Fe−Fe Dimer. We sought to study the speciation of precatalyst mixtures via IR-SEC using an optically transparent thin layer electrochemical (OTTLE-type) cell[43,55] in the absence of exogenous acid to identify any catalytically relevant intermediates prior to the first protonation step. Initial IR-SEC experiments on the dicarbonyl adduct **1-Cp^{N3}Fe(NCMe)$^+$** under reducing conditions in an MeCN solution containing 0.25 M [^{n}Bu$_4$N][PF$_6$] resulted in no discernible CO stretches, suggesting decomposition in the absence of acid. Next, we turned our attention to IR-SEC

https://doi.org/10.1021/acscatal.3c02911
ACS Catal. 2023, 13, 13650−13662

studies on the previously reported tricarbonyl cation **1-Cp^{N3}Fe(CO)$_3^+$** which has been shown to lose one equiv CO during cathodic CV scans at an onset potential of ca. −1.45 V vs Fc$^{+/0}$.[31] Prior to applying a cathodic potential, CO stretches at 2058 and 1992 cm^{-1} are observed in a MeCN solution containing 0.25 M [^{n}Bu$_4$N][PF$_6$] (Figure 8). After applying a

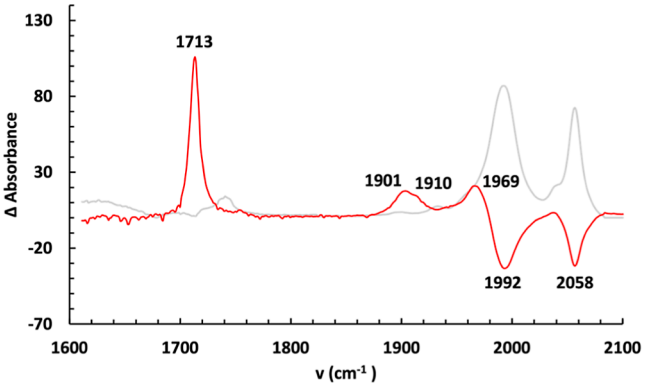

Figure 8. Difference FTIR spectra of **1-Cp^{N3}Fe(CO)$_3^+$** before (gray) and after an applied potential (red). Conditions: Ar, 1 mM **1-Cp^{N3}Fe(CO)$_3^+$**; 0.25 M [Bu$_4$][PF$_6$], MeCN solvent, Pt mesh working electrode, Pt mesh counter electrode, Ag wire pseudoreference electrode, set potential = −1.5 V vs Fc$^{+/0}$, 180 s.

potential of −1.5 V, the **1-Cp^{N3}Fe(CO)$_3^+$** bands decrease in intensity, and four new stretches appear at 1713, 1901, 1910 (sh), and 1969 cm^{-1}. Comparison of these new peaks with computed IR spectral data indicate that **1-Cp^{N3}Fe(NCMe)** and **1-Cp^{N3}Fe** are absent since the regions at 1829 and 1888 cm^{-1} are silent (Table 2). However, the CO stretching peaks for the independently prepared iron hydride complex **1-Cp^{N3}FeH** (1901, 1969 cm^{-1}; KBr) coincide with the CO stretches at 1907 and 1968 cm^{-1} produced via IR-SEC. Even though our reaction conditions rigorously exclude moisture and exogenous acid, these data indicate that the transient reduction intermediates **1-Cp^{N3}Fe(NCMe)** and/or **1-Cp^{N3}Fe** are highly reactive with trace amounts of H$^+$ in solution to generate **1-Cp^{N3}FeH**. Interestingly, the major product contains a strong CO band at 1713 cm^{-1} which is a characteristic stretching region for CO-bridged (μ_2-CO) metal complexes. Based on a reasonable match between experiment (1731, 1928 cm^{-1}) and computation (1741, 1908 cm^{-1}), theory predicts that this new product is the CO-bridged dimer **1-(Cp^{N3}Fe)$_2$** which contains two bridging and two terminal CO ligands, reminiscent of the well-known CO-bridged dimers [Fe(CO)$_2$Cp]$_2$ (Fp$_2$) and [Fe(CO)$_2$Cp*]$_2$ (Fp*$_2$).[56,57]

To further validate these spectral observations, we reacted **1-Cp^{N3}Fe(CO)$_3^+$** with 2 equiv decamethylchromocene ($E_{1/2}$(Cp*$_2$Cr) = −1.53 vs Fc$^{+/0}$, MeCN; Scheme 3, top). The nonpolar products were extracted with pentane and analyzed by ^{1}H NMR, confirming the generation of **1-Cp^{N3}FeH**, while an IR spectrum (KBr) of the polar extracts (CH$_3$CN) shows CO stretches at 1731 and 1928 cm^{-1},

Scheme 3. Synthesis of 1-(Cp^{N3}Fe)$_2$ with Observed Monomer−Dimer Equilibrium in Solution and X-ray Crystallographic Structure of 1-(Cp^{N3}Fe)$_2$ with 50% Probability Ellipsoid (Hydrogens Omitted for Clarity)

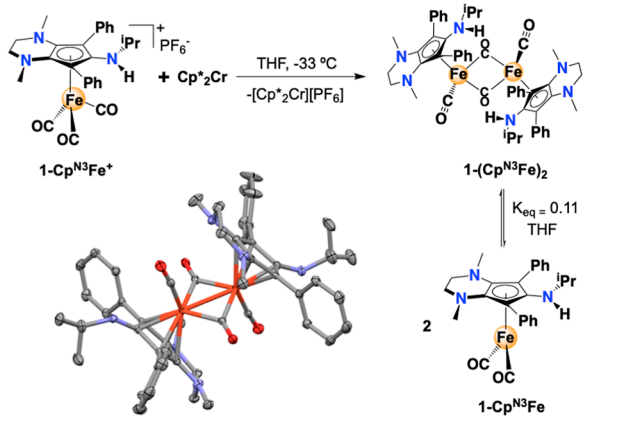

corresponding to the proposed **1-(Cp^{N3}Fe)$_2$**, as observed by IR-SEC. After working up the polar extracts, dark red-brown X-ray quality crystals were grown from a deep green solution, verifying the structure of the carbonyl-bridged dimer **1-(Cp^{N3}Fe)$_2$** (Scheme 3, bottom). Although the complex is unambiguously dimeric in the crystalline state, a solid-state IR spectrum of the crystals (KBr pellet) shows two additional sets of CO stretches (1895, 1980 cm^{-1}; Figure S2), which correlate with the DFT-computed values for monomeric **1-Cp^{N3}Fe** (Table 2). The bulkier nature of the Cp^{N3} ligand framework likely promotes dissociation to monomeric **1-Cp^{N3}Fe**, since it is known that the bulky peralkylated ligand C$_5$^{i}Pr$_5$ yields [Fe(CO)$_2$Cp^{iPr}]$_2$ in the solid state but fully dissociates into paramagnetic Fe(CO)$_2$Cp^{iPr} in solution.[58]

To investigate the possibility of a monomer−dimer equilibrium, a known mass of **1-(Cp^{N3}Fe)$_2$** was dissolved in 0.5 mL of THF-d_8 in the presence of a known concentration of the internal standard (1,3,5-trimethoxybenzene; Figure S13). Based on the well-resolved signals corresponding to diamagnetic **1-(Cp^{N3}Fe)$_2$**, the actual concentration was indeed much lower than expected, indicating that the NMR-silent **1-Cp^{N3}Fe** is present. Using these data, a monomer−dimer equilibrium constant was calculated (K_{eq} = 0.11), indicating that the dimer is slightly favored at room temperature (Scheme 3). Variable temperature UV−vis spectra in THF were obtained between 0 and 60 °C, revealing decreases in intensity at 478 and 591 nm, suggesting that the equilibrium is being shifted toward the monomer at elevated temperatures (Figure S15). Preliminary EPR data show no signals at 77 K due to exclusive formation of the dimer, while a broad anisotropic signal is observed at room temperature (deep green solution), qualitatively consistent with the NMR-derived equilibrium constant and UV−vis spectroscopic data.

Importantly, electrochemical experiments were conducted to determine if the equilibrium mixture or **1-(Cp^{N3}Fe)$_2$/1-Cp^{N3}Fe** is electrocatalytically active for H$_2$ production in the

Table 2. Experimental and Computational IR Data for Selected Fe Complexes[a]

1-Cp^{N3}Fe(CO)$_3^+$	1-Cp^{N3}Fe(NCMe)	1-Cp^{N3}Fe	1-(Cp^{N3}Fe)$_2$	1-Cp^{N3}FeH	1-(*endo*-Cp^{N3}H)Fe(CO)$_3$
1992, 2058 (1997, 2065)	(1825, 1893)	1895, 1986 (1883, 1955)	1731, 1928 (1741, 1908)	1907, 1968 (1910, 1978)	1975, 1896, 1886 (1985, 1906, 1892)

[a]Values provided in cm^{-1} with computational data provided in parentheses.

https://doi.org/10.1021/acscatal.3c02911
ACS Catal. 2023, 13, 13650−13662

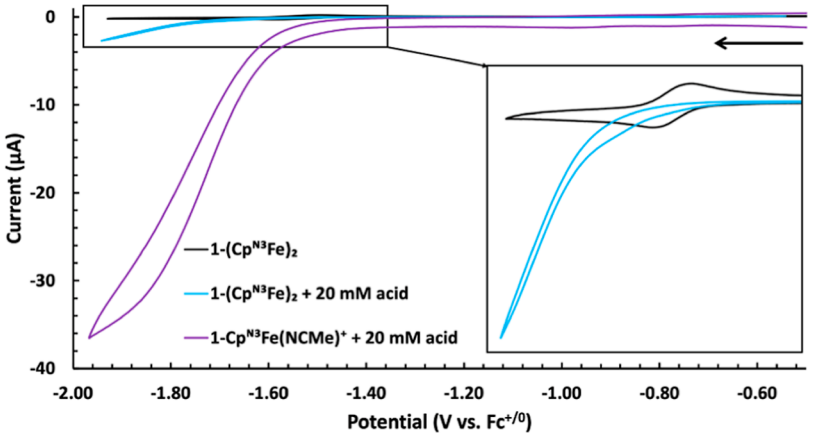

Figure 9. IUPAC plotted, *iR* uncompensated CV traces of **1-(Cp^{N3}Fe)$_2$** (black trace), **1-(Cp^{N3}Fe)$_2$** with 20 mM Tos_2NH (blue trace), and **1-Cp^{N3}Fe(NCMe)$^+$** with 20 mM Tos_2NH (purple) at 1000 mV/s. Inset: CV traces of **1-(Cp^{N3}Fe)$_2$** (black) and **1-(Cp^{N3}Fe)$_2$** with 20 mM Tos_2NH (blue). Conditions: Ar, MeCN solvent, 0.1 M $[Bu_4N][PF_6]$, 1.0 mM analyte, PEEK-encased glassy carbon working electrode, type 2 glassy carbon rod counter electrode, Ag/AgCl pseudoreference electrode in a frit-separated (CoralPor) glass compartment containing solvent and electrolyte. Initial scan direction and starting position are indicated with a black arrow.

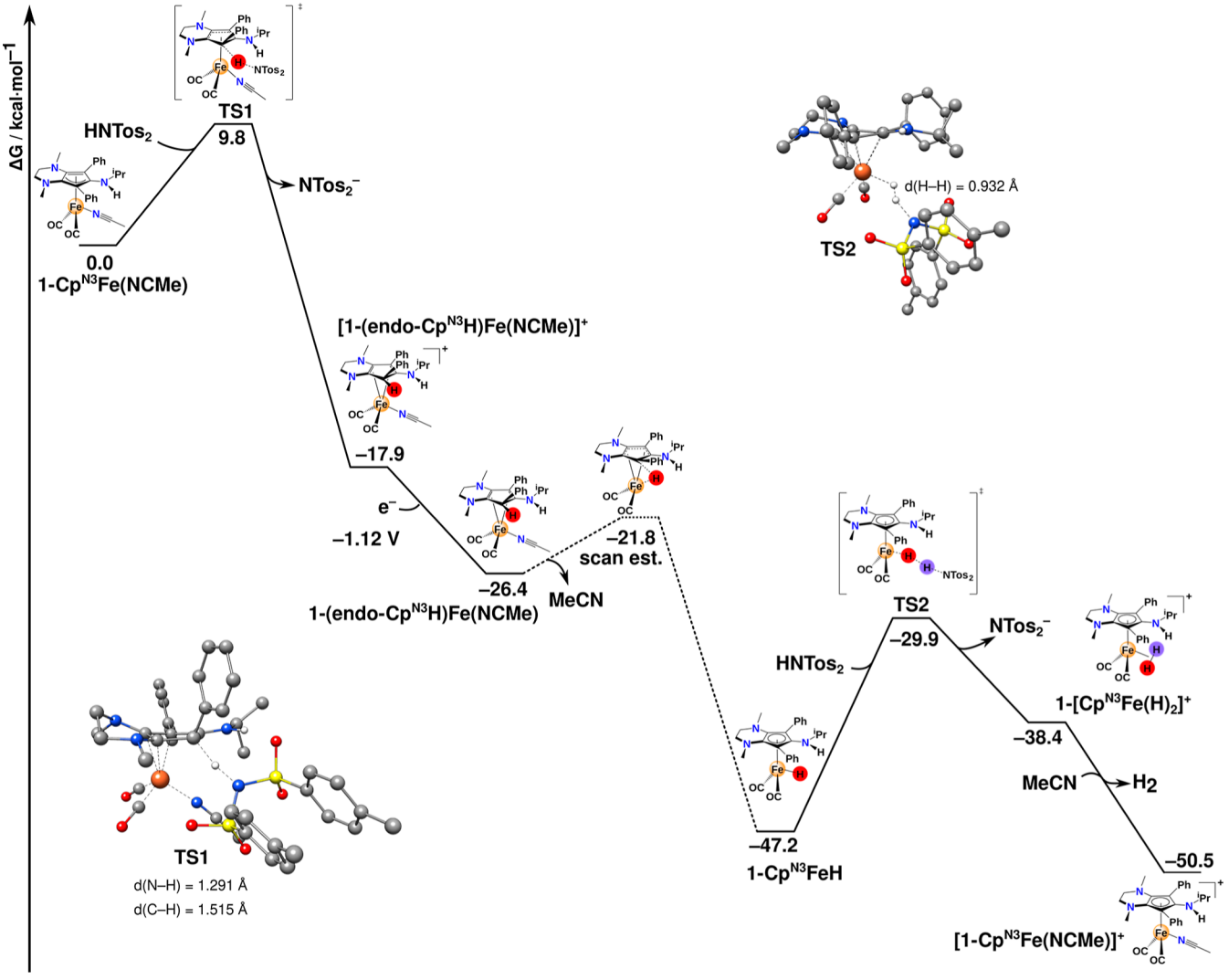

Figure 10. Free-energy profile for H_2 production relative to **1-Cp^{N3}Fe(NCMe)** given in kcal/mol with an applied external potential of −1.49 V (calculated redox potential of **[1-Cp^{N3}Fe(NCMe)]$^{+/0}$**). The barrier for the MeCN dissociation followed by proton transfer from **1-(*endo*-Cp^{N3}H)Fe(NCMe)** was estimated by a relaxed potential energy scan (see Figure 6) because no transition state could be obtained.

https://doi.org/10.1021/acscatal.3c02911
ACS Catal. 2023, 13, 13650−13662

presence of exogenous acid. First, crystals of **1-$(Cp^{N3}Fe)_2$** were dissolved in acetonitrile for CV analysis, showing partially reversible redox behavior which becomes reversible at higher scan rates (Figure S23), with a redox potential at $E_{1/2}$ = −1.53 V (Figure 9, black trace, inset). We ascribe this to be the **1-Cp^{N3}Fe/1-$Cp^{N3}Fe^-$** redox couple, which is in excellent agreement with theory ($E_{1/2}$ = −1.48 V). Consistent with our earlier report,[31] the observed irreversible oxidation peak at E_{pa} = −0.63 V in the CV trace is consistent with irreversible MeCN coordination after oxidation of **1-Cp^{N3}Fe** to **1-$Cp^{N3}Fe^+$**, generating **1-Cp^{N3}Fe(NCMe)$^+$** (Figure S24). The addition of 20 mM Tos_2NH to **1-$(Cp^{N3}Fe)_2$** shows a very modest current enhancement at ca. −1.6 V (Figure 9, blue trace). When compared with **1-Cp^{N3}Fe(NCMe)$^+$** in the presence of 20 mM Tos_2NH (Figure 9, purple trace), **1-Cp^{N3}Fe/1-$Cp^{N3}Fe^-$** are incapable of directly entering the catalytic cycle and enabling rapid H_2 production. Therefore, **1-$(Cp^{N3}Fe)_2$** and **1-Cp^{N3}Fe** are off-cycle intermediates that may form to some extent during the electrocatalytic production of H_2 but are not directly responsible for rapid catalysis.

Putting Together the Computed Mechanism. The free energies for the computed H_2 electrocatalytic mechanism are computed with an external applied potential of −1.49 V (the calculated redox potential of **1-Cp^{N3}Fe(NCMe)$^{+/0}$**), enabling the 1e$^-$ reduction of **1-Cp^{N3}Fe(NCMe)$^+$** and setting **1-Cp^{N3}Fe(NCMe)** to 0.0 kcal/mol (Figure 10). Geometries were optimized in the Turbomole[59] V. 7.5.1 program package on the efficient r^{2}SCAN-3c[60] level of theory with the implicit COSMO[61] solvation model for acetonitrile. With this level of theory, initial guesses for the transition states were obtained with the DE-GSM[62,63] method and then optimized in Turbomole. Single-point energy calculations were conducted in ORCA[50] 5.0.3 with the r^{2}SCAN0-D4[41,64,65] functional employing the large def2-QZVPP basis set.[66] This method was selected based on its robust performance for benchmark sets of organometallic reaction energies (MOR41[67] and ROST61[68]) and barrier heights (MOBH35[69]). Thermostatistical corrections were obtained with the mRRHO[70] scheme based on analytical frequencies, and solvation corrections to the final free energy were obtained with COSMO-RS[71,72] (see Supporting Information for details). After 1e$^-$ reduction of **1-Cp^{N3}Fe(NCMe)$^+$** to yield **1-Cp^{N3}Fe(NCMe)**, the initial protonation occurs with a reaction free-energy barrier of 9.8 kcal/mol (**TS1**), yielding the protonated species **1-(*endo*-Cp^{N3}H)Fe(NCMe)$^+$** in an exergonic reaction (ΔG = −17.9 kcal/mol). This species is then reduced to yield **1-(*endo*-Cp^{N3}H)Fe(NCMe)** (ΔG = −26.4 kcal/mol, with an external potential of −1.49 V) and in a follow-up step dissociates the MeCN ligand followed by ligand-to-metal proton transfer with a barrier of ΔG = 4.6 kcal/mol estimated by a relaxed surface scan (see Figure 6), yielding **1-Cp^{N3}FeH** (ΔG = −47.2 kcal/mol). The second protonation step occurs directly at **1-Cp^{N3}FeH** with a barrier of 17.2 kcal/mol (**TS2**) producing **1-$Cp^{N3}Fe(H_2)^+$** (ΔG = −38.4 kcal/mol), which releases H_2 and coordinates solvent to give **1-Cp^{N3}Fe(NCMe)$^+$**. Protonation of the amine is possible for **1-Cp^{N3}Fe** and **1-Cp^{N3}FeH** but the subsequent barriers for intramolecular proton transfer are too high in free energy (Figures S29 and S30).

CONCLUSIONS

We have presented a detailed mechanistic analysis of electrocatalytic H_2 production using Fe complexes containing amine-rich Cp^{N3} ligands using a blend of experimental techniques and state-of-the-art DFT calculations. Although it is still relatively uncommon for Cp ligands to behave as chemically noninnocent moieties, we demonstrate that regio- and stereoselective ligand protonation occurs at the Cp^{N3} ring, breaking its η^5-Cp^{N3} hapticity to generate a coordinated η^4-H moiety. Surprisingly, the coordination of inner-sphere solvent (acetonitrile) to the Fe center is crucial for electrocatalysis, effectively lowering the Cp ring protonation barrier and enabling rapid ligand-to-metal proton migration to generate an FeH complex. Using other nitrogen-based donor solvents inhibits catalysis. Synthesis of an isoelectronic (η^4-H)Fe complex containing an inner-sphere CO ligand in place of acetonitrile also renders the system inert, as the ligand-to-metal proton transfer is kinetically insurmountable due to the high CO ligand dissociation energy. Independent synthesis of on-cycle (Cp^{N3})FeH intermediates shows that protonation in the presence of exogenous acid furnishes high yields of H_2; DFT calculations indicate that direct (Cp^{N3})FeH protonation is the TOF-determining step during catalysis. As more Cp-based systems are reported that demonstrate chemical noninnocence in proton-coupled electron transfer (PCET) chemistry, we hope that broader trends will be uncovered to better understand the kinetic origins of metal vs Cp ligand protonation for the efficient reduction of protons and other chemical fuel precursors.

ASSOCIATED CONTENT

Supporting Information

The Supporting Information is available free of charge at https://pubs.acs.org/doi/10.1021/acscatal.3c02911.

General comments; syntheses; IR, NMR, and UV-vis spectra; electrochemistry; NMR kinetics; and computational details (PDF)

Computed structures and energies (ZIP)

Crystallographic data for CCDC 2271971 (CIF)

Crystallographic data for CCDC 2271972 (CIF)

Crystallographic data for CCDC 2271973 (CIF)

Crystallographic data for CCDC 2271974 (CIF)

Crystallographic data for CCDC 2271975 (CIF)

AUTHOR INFORMATION

Corresponding Authors

Andreas Hansen − *Mulliken Center for Theoretical Chemistry, Clausius-Institut für Physikalische und Theoretische Chemie, Rheinische Friedrich-Wilhelms-Universität Bonn, Bonn 53115, Germany;* orcid.org/0000-0003-1659-8206; Email: hansen@thch.uni-bonn.de

Demyan E. Prokopchuk − *Department of Chemistry, Rutgers University-Newark, Newark, New Jersey 07102, United States;* orcid.org/0000-0002-6352-3509; Email: demyan.prokopchuk@rutgers.edu

Authors

Bhumika Goel − *Department of Chemistry, Rutgers University-Newark, Newark, New Jersey 07102, United States*

Hagen Neugebauer − *Mulliken Center for Theoretical Chemistry, Clausius-Institut für Physikalische und Theoretische Chemie, Rheinische Friedrich-Wilhelms-Universität Bonn, Bonn 53115, Germany;* orcid.org/0000-0003-1309-0503

https://doi.org/10.1021/acscatal.3c02911
ACS Catal. 2023, 13, 13650−13662

Andrew I. VanderWeide − *Department of Chemistry, Rutgers University-Newark, Newark, New Jersey 07102, United States*

Práxedes Sánchez − *Department of Chemistry, Rutgers University-Newark, Newark, New Jersey 07102, United States*

Roger A. Lalancette − *Department of Chemistry, Rutgers University-Newark, Newark, New Jersey 07102, United States;* orcid.org/0000-0002-3470-532X

Stefan Grimme − *Mulliken Center for Theoretical Chemistry, Clausius-Institut für Physikalische und Theoretische Chemie, Rheinische Friedrich-Wilhelms-Universität Bonn, Bonn 53115, Germany;* orcid.org/0000-0002-5844-4371

Complete contact information is available at: https://pubs.acs.org/10.1021/acscatal.3c02911

Notes

The authors declare no competing financial interest.

■ ACKNOWLEDGMENTS

D.E.P. thanks the National Science Foundation (NSF) for support under Grant 2055097, and S.G. thanks the Deutsche Forschungsgemeinschaft under Grant 1927/16-1. This research was also supported by a Rutgers University-Newark startup grant (to D.E.P.). X-ray structural solutions were partly supported by the NSF under Grant 2018753. Supplemental funding for this project was provided by the Rutgers University—Newark Chancellor's Research Office.

■ REFERENCES

(1) Bullock, R. M.; Chen, J. G.; Gagliardi, L.; Chirik, P. J.; Farha, O. K.; Hendon, C. H.; Jones, C. W.; Keith, J. A.; Klosin, J.; Minteer, S. D.; Morris, R. H.; Radosevich, A. T.; Rauchfuss, T. B.; Strotman, N. A.; Vojvodic, A.; Ward, T. R.; Yang, J. Y.; Surendranath, Y. Using nature's blueprint to expand catalysis with Earth-abundant metals. *Science* **2020**, *369* (6505), No. eabc3183.

(2) Hansen, J. N.; Prats, H.; Toudahl, K. K.; Mørch Secher, N.; Chan, K.; Kibsgaard, J.; Chorkendorff, I. Is There Anything Better than Pt for HER? *ACS Energy Lett.* **2021**, *6* (4), 1175−1180.

(3) Chong, L.; Wen, J.; Kubal, J.; Sen, F. G.; Zou, J.; Greeley, J.; Chan, M.; Barkholtz, H.; Ding, W.; Liu, D.-J. Ultralow-loading platinum-cobalt fuel cell catalysts derived from imidazolate frameworks. *Science* **2018**, *362* (6420), 1276−1281.

(4) Sandbeck, D. J. S.; Secher, N. M.; Speck, F. D.; Sørensen, J. E.; Kibsgaard, J.; Chorkendorff, I.; Cherevko, S. Particle Size Effect on Platinum Dissolution: Considerations for Accelerated Stability Testing of Fuel Cell Catalysts. *ACS Catal.* **2020**, *10* (11), 6281−6290.

(5) Lubitz, W.; Ogata, H.; Rüdiger, O.; Reijerse, E. Hydrogenases. *Chem. Rev.* **2014**, *114* (8), 4081−4148.

(6) Evans, R. M.; Brooke, E. J.; Wehlin, S. A. M.; Nomerotskaia, E.; Sargent, F.; Carr, S. B.; Phillips, S. E. V.; Armstrong, F. A. Mechanism of hydrogen activation by [NiFe] hydrogenases. *Nat. Chem. Biol.* **2016**, *12*, 46−50.

(7) Wodrich, M. D.; Hu, X. Natural inspirations for metal-ligand cooperative catalysis. *Nat. Rev. Chem* **2017**, *2*, 0099.

(8) Helm, M. L.; Stewart, M. P.; Bullock, R. M.; DuBois, M. R.; DuBois, D. L. A Synthetic Nickel Electrocatalyst with a Turnover Frequency Above 100,000 s^{-1} for H_2 Production. *Science* **2011**, *333* (6044), 863−866.

(9) Wiedner, E. S.; Appel, A. M.; Raugei, S.; Shaw, W. J.; Bullock, R. M. Molecular Catalysts with Diphosphine Ligands Containing Pendant Amines. *Chem. Rev.* **2022**, *122* (14), 12427−12474.

(10) O'Hagan, M.; Ho, M.-H.; Yang, J. Y.; Appel, A. M.; DuBois, M. R.; Raugei, S.; Shaw, W. J.; DuBois, D. L.; Bullock, R. M. Proton Delivery and Removal in $[Ni(PR_2NR'_2)_2]^{2+}$ Hydrogen Production and Oxidation Catalysts. *J. Am. Chem. Soc.* **2012**, *134* (47), 19409−19424.

(11) Rauchfuss, T. B. Diiron Azadithiolates as Models for the [FeFe]-Hydrogenase Active Site and Paradigm for the Role of the Second Coordination Sphere. *Acc. Chem. Res.* **2015**, *48* (7), 2107−2116.

(12) Schilter, D.; Camara, J. M.; Huynh, M. T.; Hammes-Schiffer, S.; Rauchfuss, T. B. Hydrogenase Enzymes and Their Synthetic Models: The Role of Metal Hydrides. *Chem. Rev.* **2016**, *116* (15), 8693−8749.

(13) Bullock, R. M.; Chen, J. G.; Gagliardi, L.; Chirik, P. J.; Farha, O. K.; Hendon, C. H.; Jones, C. W.; Keith, J. A.; Klosin, J.; Minteer, S. D.; Morris, R. H.; Radosevich, A. T.; Rauchfuss, T. B.; Strotman, N. A.; Vojvodic, A.; Ward, T. R.; Yang, J. Y.; Surendranath, Y. Using nature's blueprint to expand catalysis with Earth-abundant metals. *Science* **2020**, *369* (6505), No. eabc3183.

(14) Nichols, A. W.; Hooe, S. L.; Kuehner, J. S.; Dickie, D. A.; Machan, C. W. Electrocatalytic CO2 Reduction to Formate with Molecular Fe(III) Complexes Containing Pendent Proton Relays. *Inorg. Chem.* **2020**, *59* (9), 5854−5864.

(15) Rønne, M. H.; Cho, D.; Madsen, M. R.; Jakobsen, J. B.; Eom, S.; Escoudé, É.; Hammershøj, H. C. D.; Nielsen, D. U.; Pedersen, S. U.; Baik, M.-H.; Skrydstrup, T.; Daasbjerg, K. Ligand-Controlled Product Selectivity in Electrochemical Carbon Dioxide Reduction Using Manganese Bipyridine Catalysts. *J. Am. Chem. Soc.* **2020**, *142* (9), 4265−4275.

(16) Chapovetsky, A.; Welborn, M.; Luna, J. M.; Haiges, R.; Miller, T. F., III; Marinescu, S. C. Pendant Hydrogen-Bond Donors in Cobalt Catalysts Independently Enhance CO2 Reduction. *ACS Cent. Sci.* **2018**, *4* (3), 397−404.

(17) Chapovetsky, A.; Do, T. H.; Haiges, R.; Takase, M. K.; Marinescu, S. C. Proton-Assisted Reduction of CO_2 by Cobalt Aminopyridine Macrocycles. *J. Am. Chem. Soc.* **2016**, *138* (18), 5765−5768.

(18) Queyriaux, N.; Sun, D.; Fize, J.; Pécaut, J.; Field, M. J.; Chavarot-Kerlidou, M.; Artero, V. Electrocatalytic Hydrogen Evolution with a Cobalt Complex Bearing Pendant Proton Relays: Acid Strength and Applied Potential Govern Mechanism and Stability. *J. Am. Chem. Soc.* **2020**, *142* (1), 274−282.

(19) Roy, S.; Sharma, B.; Pécaut, J.; Simon, P.; Fontecave, M.; Tran, P. D.; Derat, E.; Artero, V. Molecular Cobalt Complexes with Pendant Amines for Selective Electrocatalytic Reduction of Carbon Dioxide to Formic Acid. *J. Am. Chem. Soc.* **2017**, *139* (10), 3685−3696.

(20) Nichols, A. W.; Machan, C. W. Secondary-Sphere Effects in Molecular Electrocatalytic CO_2 Reduction. *Front. Chem.* **2019**, *7*, 397.

(21) Savéant, J. Proton Relays in Molecular Catalysis of Electrochemical Reactions: Origin and Limitations of the Boosting Effect. *Angew. Chem., Int. Ed.* **2019**, *58* (7), 2125−2128.

(22) Raugei, S.; DuBois, D. L.; Rousseau, R.; Chen, S.; Ho, M.-H.; Bullock, R. M.; Dupuis, M. Toward Molecular Catalysts by Computer. *Acc. Chem. Res.* **2015**, *48* (2), 248−255.

(23) Warburton, R. E.; Soudackov, A. V.; Hammes-Schiffer, S. Theoretical Modeling of Electrochemical Proton-Coupled Electron Transfer. *Chem. Rev.* **2022**, *122* (12), 10599−10650.

(24) Bursch, M.; Mewes, J.-M.; Hansen, A.; Grimme, S. Best-Practice DFT Protocols for Basic Molecular Computational Chemistry. *Angew. Chem., Int. Ed.* **2022**, *61* (42), No. e202205735.

(25) VanderWeide, A.; Prokopchuk, D. E. Cyclopentadienyl ring activation in organometallic chemistry and catalysis. *Nat. Rev. Chem* **2023**, *7*, 561−572.

(26) Chalkley, M. J.; Del Castillo, T. J.; Matson, B. D.; Roddy, J. P.; Peters, J. C. Catalytic N_2-to-NH_3 Conversion by Fe at Lower Driving Force: A Proposed Role for Metallocene-Mediated PCET. *ACS Cent. Sci.* **2017**, *3* (3), 217−223.

(27) Chalkley, M. J.; Del Castillo, T. J.; Matson, B. D.; Peters, J. C. Fe-Mediated Nitrogen Fixation with a Metallocene Mediator: Exploring pKa Effects and Demonstrating Electrocatalysis. *J. Am. Chem. Soc.* **2018**, *140* (19), 6122−6129.

(28) Chalkley, M. J.; Oyala, P. H.; Peters, J. C. Cp* Noninnocence Leads to a Remarkably Weak C-H Bond via Metallocene Protonation. *J. Am. Chem. Soc.* **2019**, *141* (11), 4721−4729.
(29) Kurtz, D. A.; Dhar, D.; Elgrishi, N.; Kandemir, B.; McWilliams, S. F.; Howland, W. C.; Chen, C.-H.; Dempsey, J. L. Redox-Induced Structural Reorganization Dictates Kinetics of Cobalt(III) Hydride Formation via Proton-Coupled Electron Transfer. *J. Am. Chem. Soc.* **2021**, *143* (9), 3393−3406.
(30) Henke, W. C.; Peng, Y.; Meier, A. A.; Fujita, E.; Grills, D. C.; Polyansky, D. E.; Blakemore, J. D. Mechanistic roles of metal- and ligand-protonated species in hydrogen evolution with [Cp*Rh] complexes. *Proc. Natl. Acad. Sci. U.S.A.* **2023**, *120* (21), No. e2217189120.
(31) Sánchez, P.; Goel, B.; Neugebauer, H.; Lalancette, R. A.; Grimme, S.; Hansen, A.; Prokopchuk, D. E. Ligand Protonation at Carbon, not Nitrogen, during H2 Production with Amine-Rich Iron Electrocatalysts. *Inorg. Chem.* **2021**, *60* (22), 17407−17413.
(32) Kütt, A.; Tshepelevitsh, S.; Saame, J.; Lõkov, M.; Kaljurand, I.; Selberg, S.; Leito, I. Strengths of Acids in Acetonitrile. *Eur. J. Org Chem.* **2021**, *2021* (9), 1407−1419.
(33) McCarthy, B. D.; Martin, D. J.; Rountree, E. S.; Ullman, A. C.; Dempsey, J. L. Electrochemical Reduction of Brønsted Acids by Glassy Carbon in Acetonitrile—Implications for Electrocatalytic Hydrogen Evolution. *Inorg. Chem.* **2014**, *53* (16), 8350−8361.
(34) To the best of our knowledge, the homoconjugation effects of bis(arylsulfonyl)imide acids in acetonitrile have not been investigated.
(35) Kaeffer, N.; Morozan, A.; Fize, J.; Martinez, E.; Guetaz, L.; Artero, V. The Dark Side of Molecular Catalysis: Diimine-Dioxime Cobalt Complexes Are Not the Actual Hydrogen Evolution Electrocatalyst in Acidic Aqueous Solutions. *ACS Catal.* **2016**, *6* (6), 3727−3737.
(36) Lee, K. J.; McCarthy, B. D.; Dempsey, J. L. On decomposition, degradation, and voltammetric deviation: the electrochemist's field guide to identifying precatalyst transformation. *Chem. Soc. Rev.* **2019**, *48*, 2927−2945.
(37) Gómez-Gallego, M.; Sierra, M. A. Kinetic Isotope Effects in the Study of Organometallic Reaction Mechanisms. *Chem. Rev.* **2011**, *111* (8), 4857−4963.
(38) Fey, N.; Lynam, J. M. Computational mechanistic study in organometallic catalysis: Why prediction is still a challenge. *WIREs Computational Molecular Science* **2022**, *12* (4), No. e1590.
(39) Iron, M. A.; Janes, T. Evaluating Transition Metal Barrier Heights with the Latest Density Functional Theory Exchange-Correlation Functionals: The MOBH35 Benchmark Database. *J. Phys. Chem. A* **2019**, *123* (17), 3761−3781.
(40) Iron, M. A.; Janes, T. Correction to "Evaluating Transition Metal Barrier Heights with the Latest Density Functional Theory Exchange-Correlation Functionals: The MOBH35 Benchmark Database. *J. Phys. Chem. A* **2019**, *123* (29), 6379−6380.
(41) Bursch, M.; Neugebauer, H.; Ehlert, S.; Grimme, S. Dispersion corrected r^2SCAN based global hybrid functionals: r^2SCANh, rSCAN0, and r^2SCAN50. *J. Chem. Phys.* **2022**, *156* (13), 134105.
(42) Appel, A. M.; Helm, M. L. Determining the Overpotential for a Molecular Electrocatalyst. *ACS Catal.* **2014**, *4* (2), 630−633.
(43) Lee, K. J.; Elgrishi, N.; Kandemir, B.; Dempsey, J. L. Electrochemical and spectroscopic methods for evaluating molecular electrocatalysts. *Nat. Rev. Chem* **2017**, *1* (5), 0039.
(44) Patel, D.; Wooles, A.; Cornish, A. D.; Steven, L.; Davies, E. S.; Evans, D. J.; McMaster, J.; Lewis, W.; Blake, A. J.; Liddle, S. T. Synthesis and characterisation of halide, separated ion pair, and hydride cyclopentadienyl iron bis(diphenylphosphino)ethane derivatives. *Dalton Trans.* **2015**, *44* (31), 14159−14177.
(45) Hu, Y.; Shaw, A. P.; Estes, D. P.; Norton, J. R. Transition-Metal Hydride Radical Cations. *Chem. Rev.* **2016**, *116* (15), 8427−8462.
(46) Peng, Y.; Ramos-Garcés, M. V.; Lionetti, D.; Blakemore, J. D. Structural and Electrochemical Consequences of [Cp*] Ligand Protonation. *Inorg. Chem.* **2017**, *56* (17), 10824−10831.
(47) Davison, A.; Green, M. L. H.; Wilkinson, G. 620. π-Cyclopentadienyl- and cyclopentadiene-iron carbonyl complexes. *J. Chem. Soc.* **1961**, *0* (0), 3172−3177.
(48) Hamon, P.; Hamon, J. R.; Lapinte, C. Isolation and characterization of a cationic 19-electron iron(III) hydride complex; electron transfer induced hydride migration by carbon monoxide at an iron(III) centre. *J. Chem. Soc., Chem. Commun.* **1992**, 1602.
(49) Schild, D. J.; Drover, M. W.; Oyala, P. H.; Peters, J. C. Generating Potent C-H PCET Donors: Ligand-Induced Fe-to-Ring Proton Migration from a Cp*Fe(III)-H Complex Demonstrates a Promising Strategy. *J. Am. Chem. Soc.* **2020**, *142* (44), 18963−18970.
(50) Neese, F. Software update: The ORCA program system—Version 5.0. *WIREs Computational Molecular Science* **2022**, *12* (5), No. e1606.
(51) Adamo, C.; Barone, V. Toward reliable density functional methods without adjustable parameters: The PBE0 model. *J. Chem. Phys.* **1999**, *110* (13), 6158−6170.
(52) Grimme, S.; Antony, J.; Ehrlich, S.; Krieg, H. A consistent and accurate ab initio parametrization of density functional dispersion correction (DFT-D) for the 94 elements H-Pu. *J. Chem. Phys.* **2010**, *132* (15), 154104.
(53) Grimme, S.; Ehrlich, S.; Goerigk, L. Effect of the damping function in dispersion corrected density functional theory. *J. Comput. Chem.* **2011**, *32* (7), 1456−1465.
(54) Cossi, M.; Rega, N.; Scalmani, G.; Barone, V. Energies, structures, and electronic properties of molecules in solution with the C-PCM solvation model. *J. Comput. Chem.* **2003**, *24* (6), 669−681.
(55) Krejčik, M.; Daněk, M.; Hartl, F. Simple construction of an infrared optically transparent thin-layer electrochemical cell: Applications to the redox reactions of ferrocene, $Mn_2(CO)_{10}$ and $Mn(CO)_3$(3,5-di-t-butyl-catecholate)-. *J. Electroanal. Chem. Interfacial Electrochem.* **1991**, *317* (1−2), 179−187.
(56) Teller, R. G.; Williams, J. M. Crystal and molecular structure of bis[dicarbonyl(π-pentamethylcyclopentadienyl)iron], $(\eta^5\text{-}C_5Me_5)_2Fe_2(CO)_4$, and structural comparisons with the nonmethylated analog. *Inorg. Chem.* **1980**, *19* (9), 2770−2773.
(57) Mills, O. S. Studies of some Carbon Compounds of the Transition Metals. I. The Crystal Structure of Dicyclopentadienyldiiron Tetracarbonyl. *Acta Crystallogr.* **1958**, *11*, 620−623.
(58) Sitzmann, H.; Dezember, T.; Kaim, W.; Baumann, F.; Stalke, D.; Kärcher, J.; Dormann, E.; Winter, H.; Wachter, C.; Kelemen, M. Synthesis and Characterization of the Stable Dicarbonyl(cyclopentadienyl)iron Radical $[(C_5R_5)Fe(CO)_2]$ (R = $CHMe_2$). *Angew Chem. Int. Ed. Engl.* **1996**, *35* (23−24), 2872−2875.
(59) TURBOMOLE. TURBOMOLE V7.5. http://www.turbomole.org.
(60) Grimme, S.; Hansen, A.; Ehlert, S.; Mewes, J.-M. r2SCAN-3c: A "Swiss army knife" composite electronic-structure method. *J. Chem. Phys.* **2021**, *154* (6), 064103.
(61) Klamt, A.; Schüürmann, G. COSMO: a new approach to dielectric screening in solvents with explicit expressions for the screening energy and its gradient. *J. Chem. Soc., Perkin Trans. 2* **1993**, No. 5, 799−805.
(62) Zimmerman, P. M. Growing string method with interpolation and optimization in internal coordinates: method and examples. *J. Chem. Phys.* **2013**, *138* (18), 184102.
(63) Zimmerman, P. Reliable Transition State Searches Integrated with the Growing String Method. *J. Chem. Theory Comput.* **2013**, *9* (7), 3043−3050.
(64) Caldeweyher, E.; Bannwarth, C.; Grimme, S. Extension of the D3 dispersion coefficient model. *J. Chem. Phys.* **2017**, *147* (3), 034112.
(65) Caldeweyher, E.; Ehlert, S.; Hansen, A.; Neugebauer, H.; Spicher, S.; Bannwarth, C.; Grimme, S. A generally applicable atomic-charge dependent London dispersion correction. *J. Chem. Phys.* **2019**, *150* (15), 154122.
(66) Weigend, F.; Ahlrichs, R. Balanced basis sets of split valence, triple zeta valence and quadruple zeta valence quality for H to Rn:

https://doi.org/10.1021/acscatal.3c02911
ACS Catal. 2023, 13, 13650−13662

Design and assessment of accuracy. *Phys. Chem. Chem. Phys.* **2005**, *7* (18), 3297−3305.
(67) Dohm, S.; Hansen, A.; Steinmetz, M.; Grimme, S.; Checinski, M. P. Comprehensive Thermochemical Benchmark Set of Realistic Closed-Shell Metal Organic Reactions. *J. Chem. Theory Comput.* **2018**, *14* (5), 2596−2608.
(68) Maurer, L. R.; Bursch, M.; Grimme, S.; Hansen, A. Assessing Density Functional Theory for Chemically Relevant Open-Shell Transition Metal Reactions. *J. Chem. Theory Comput.* **2021**, *17* (10), 6134−6151.
(69) Dohm, S.; Bursch, M.; Hansen, A.; Grimme, S. Semiautomated Transition State Localization for Organometallic Complexes with Semiempirical Quantum Chemical Methods. *J. Chem. Theory Comput.* **2020**, *16* (3), 2002−2012.
(70) Grimme, S. Supramolecular Binding Thermodynamics by Dispersion-Corrected Density Functional Theory. *Chem.—Eur. J.* **2012**, *18* (32), 9955−9964.
(71) Klamt, A. Conductor-like Screening Model for Real Solvents: A New Approach to the Quantitative Calculation of Solvation Phenomena. *J. Phys. Chem.* **1995**, *99* (7), 2224−2235.
(72) Klamt, A.; Jonas, V.; Bürger, T.; Lohrenz, J. C. W. Refinement and Parametrization of COSMO-RS. *J. Phys. Chem. A* **1998**, *102* (26), 5074−5085.

https://doi.org/10.1021/acscatal.3c02911
ACS Catal. 2023, 13, 13650−13662